

Performance and Calibration of the AXAF High Resolution Camera I: Imaging Readout

A.T. Kenter, J.H. Chappel, K. Kobayashi, R.P. Kraft, G.R. Meehan, S.S. Murray, M.V. Zombeck
Smithsonian Astrophysical Observatory, 60 Garden St., Cambridge, MA 02138

G.W. Fraser, J.F. Pearson, J.E. Lees, A.N. Brunton, S.E. Pearce
University of Leicester, Leicester, LE1 7RH, England

M. Barbera, A. Collura, S. Serio

Instituto e Osservatorio Astronomico G.S. Vaiana, Palermo, Italy, 90134

ABSTRACT

The High Resolution Camera (HRC) will be one of the two focal plane instruments on the Advanced X-ray Astrophysics Facility, (AXAF). AXAF will perform high resolution spectrometry and imaging in the X-ray band of 0.1 to 10 keV. The HRC instrument consists of two detectors, the HRC-I for imaging and the HRC-S for spectroscopy. Each HRC detector consists of a thin aluminized polyimide window, a chevron pair of microchannel plates (MCPs) and a crossed grid charge readout. The HRC-I is a 100×100 mm detector optimized for high resolution imaging and timing, the HRC-S is a $\sim 30 \times 300$ mm detector optimized to function as the readout for the Low Energy Transmission Grating Spectrometer (LETGS).

In this paper we present the absolute quantum efficiency, spatial resolution, point spread response function and count rate linearity of the HRC-I detector. Data taken at the HRC laboratory and at the Marshall Space Flight Center X-ray Calibration Facility are presented.

The development of the HRC is a collaborative effort between The Smithsonian Astrophysical Observatory, University of Leicester UK and the Osservatorio Astronomico, G.S. Vaiana, Palermo Italy.

Keywords: microchannel plate, AXAF, High Resolution Camera.

1 INTRODUCTION

The Advanced X-ray Astrophysics Facility (AXAF) is a major space observatory designed to perform high resolution imaging and spectral observations in the 0.1 to 10 keV X-ray energy band. This NASA observatory is scheduled for launch in 1998. The major observatory components are the High Resolution Mirror Assembly (HRMA), the two sets of objective transmission gratings and the two focal plane instruments. The HRMA consists of four pairs of nested Iridium coated Wolter type I optics. The objective transmission gratings consist of the Low Energy Transmission Gratings (LETG) and the High Energy Transmission Gratings (HETG). The two focal plane instruments are the AXAF CCD Imaging Spectrometer (ACIS) and the High Resolution Camera (HRC).

The HRMA has a 10 meter focal length and a plate scale of $49 \mu\text{m}$ per arc-sec. The largest paraboloid-hyperboloid pair of optics, P1H1, has a 1.2 meter diameter. The performance of the P1H1 pair was shown to individually have an imaging performance of < 0.2 arc-sec FWHM.¹ The overall HRMA performance is discussed elsewhere.²

The LETGs³ in conjunction with the HRMA and the HRC detector will perform high resolution dispersive spectroscopy with $\frac{E}{\Delta E} > 1000$ in the 0.1 to 2.0 keV X-ray band. The HETG⁴, in conjunction with the HRMA

and the ACIS, will operate in the 0.4 to 10 keV range with resolutions up to $\frac{E}{\Delta E} > 1000$.

The ACIS consists of two detectors; one for simultaneous spatial and spectral imaging, and the other primarily for reading out the HETGs. The ACIS spatial and non-dispersive spectral resolutions are 0.6 arc-sec and $\frac{E}{\Delta E} \approx 50$ @6keV, respectively.

The HRC consists of two MCP based detectors; one for high resolution large field of view imaging and a second detector which is optimized as the readout for the LETGs. The HRC detectors have spatial resolutions of < 0.5 arc-sec and limited inherent energy resolution of $\frac{E}{\Delta E} \approx 1$.

More in depth discussions of the AXAF mission have been presented elsewhere.^{5,6}

2 THE HIGH RESOLUTION CAMERA (HRC)

The HRC detectors will be the largest, lowest background-rate MCP based X-ray detectors ever flown. They are technological descendants of the highly successful Einstein and ROSAT High Resolution Imagers (HRIs).^{7,8} The HRC detectors differ from their predecessors primarily in size, geometry and electronic implementation. In addition, the HRC detectors use MCPs fabricated from low radioactive content glass and the HRC instrument employs an active cosmic ray anti-coincidence shield.

The High Resolution Camera (HRC) consists of two detectors; the HRC-I and the HRC-S. Both detectors have excellent spatial resolution ($\sim 20\mu\text{m}$ FWHM)⁹, fast event-time-tagging ($16\mu\text{sec}$) and low background ($4 \times 10^{-6} \text{ sec}^{-1} \text{ arcsec}^{-2}$)¹⁰. The HRC detectors use a CsI photocathode and thin aluminized polyimide filters to provide high detector quantum efficiency at the low energies of the AXAF band where the effective HRMA area is largest. The focal plane layout of the HRC detectors is presented in Figure 1.

The HRC-S is further optimized to act as the readout for the Low Energy Transmission Gratings (LETGs); The HRC-S has an active area of 20×300 mm and it is piecewise tilted to approximate the Rowland circle. In addition the HRC-S has a structured UV ion shield¹¹ and a Two Facet Reflection Filter (TFRF).^{9,12} The structured UVIS and the TFRF will be used to assist in spectral order sorting. In conjunction with the LETGs, the excellent spatial resolution and large size of the the HRC-S will provide outstanding spectral resolution ($\frac{E}{\Delta E} > 1000$) and spectral range extending to $\sim 160\text{\AA}$.

The HRC-I is intended for low background, large Field-of-View (FOV) high resolution imaging and timing. The HRC-I has a geometrical area of $93\text{mm} \times 93\text{mm}$. In combination with the HRMA focal length of 10m, this provides a field of view of $\sim 31 \times 31$ arc-minutes. The combination of low background, large FOV, high angular resolution and precise timing will ensure that the HRC-I has unprecedented performance as a soft X-ray faint object camera.

As depicted in Figure 2, an HRC type detector consists of a aluminized polyimide UV ion shield (UVIS); a CsI photocathode, a chevron pair of MCPs and Crossed Grid Charge Detector (CGCD) readout. The HRC instrument also employs passive and active shielding to reduce its background event rate. The UVIS blocks out-of-band ultraviolet photons and low energy ions and electrons. The CsI enhances photoelectric conversion of the X-ray photon. The two MCPs in the chevron arrangement provide electron multiplication of $\sim 2 \times 10^7$ while minimizing ion feedback. The CGCD collects the resulting electron cloud, from which the electronics determine the pulse height amplitude, arrival time, and position of the X-ray photon.

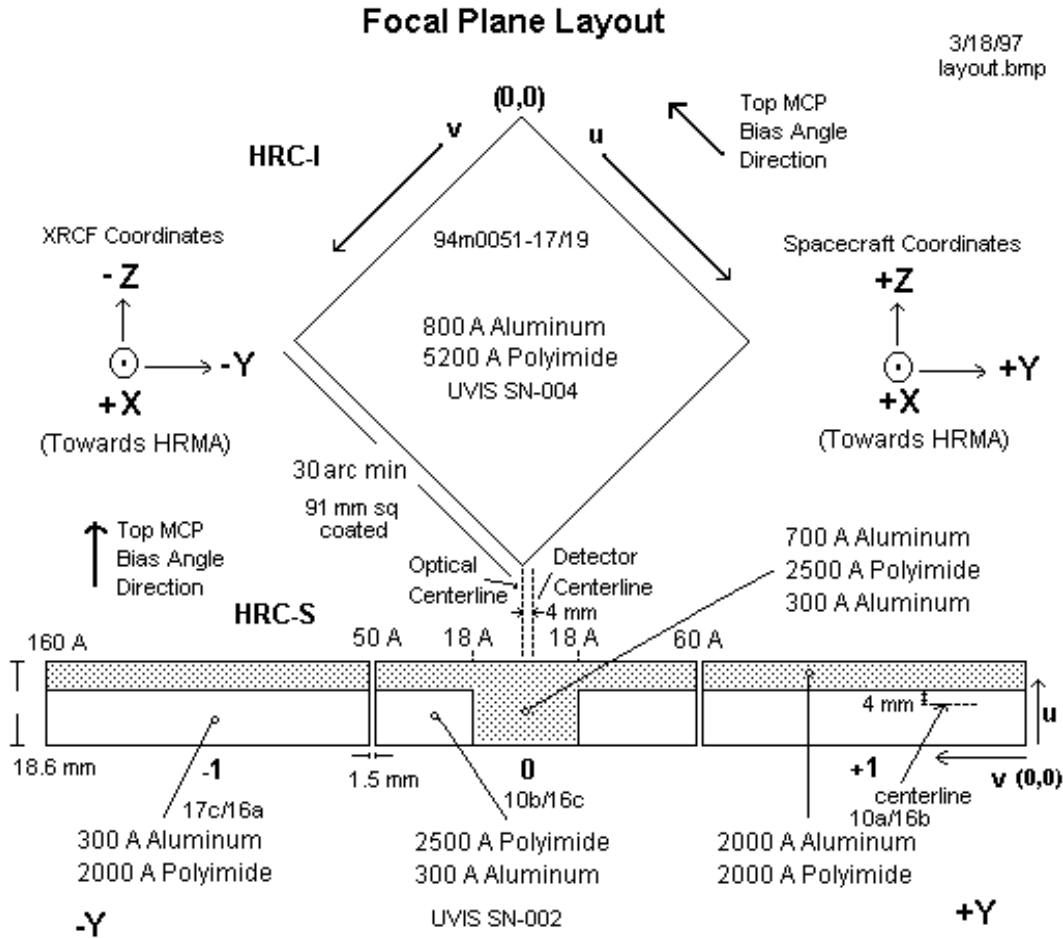


Figure 1: Focal plane layout of the HRC showing the HRC-I and HRC-S.

2.1 THE UV ION SHIELDS

The UVIS for the HRC detectors consists of an aluminized thin plastic membrane. For the HRC-I detector, the UVIS consists of 800Å aluminum vacuum deposited on a spin-cast 5200Å polyimide shield (nominal thicknesses). The HRC-I UVIS was fabricated by the Luxel Corporation of Friday Harbor, Washington.

The UV ion shield protects the sensitive photocathode from out-of-band ultra-violet light, and from low energy electrons and ions. In addition, the UVIS acts as an electrode to provide a uniform field above the top MCP surface. This uniform field performs multiple functions; it eliminates random time and spatially varying background observed in MCP detectors,¹³ and it collects photoelectrons emitted from the inter-channel MCP web. The photoelectrons emitted from the inter channel MCP web would otherwise broaden the detector point spread function.⁸

The HRC-I flight UVIS was visually examined for defects and uniformity. UV ion shields of a similar type have been examined for uniformity in areal density with soft X-ray transmission tests, and no variations on a ~ 1 mm² spatial scale were observed.¹⁴ Witness samples of the actual spin cast aluminized polyimide flight HRC-I UVIS have been extensively measured for X-ray transmission using synchrotron light sources, X-ray monochromators and alpha particle induced fluorescence sources. In addition these witness samples have been

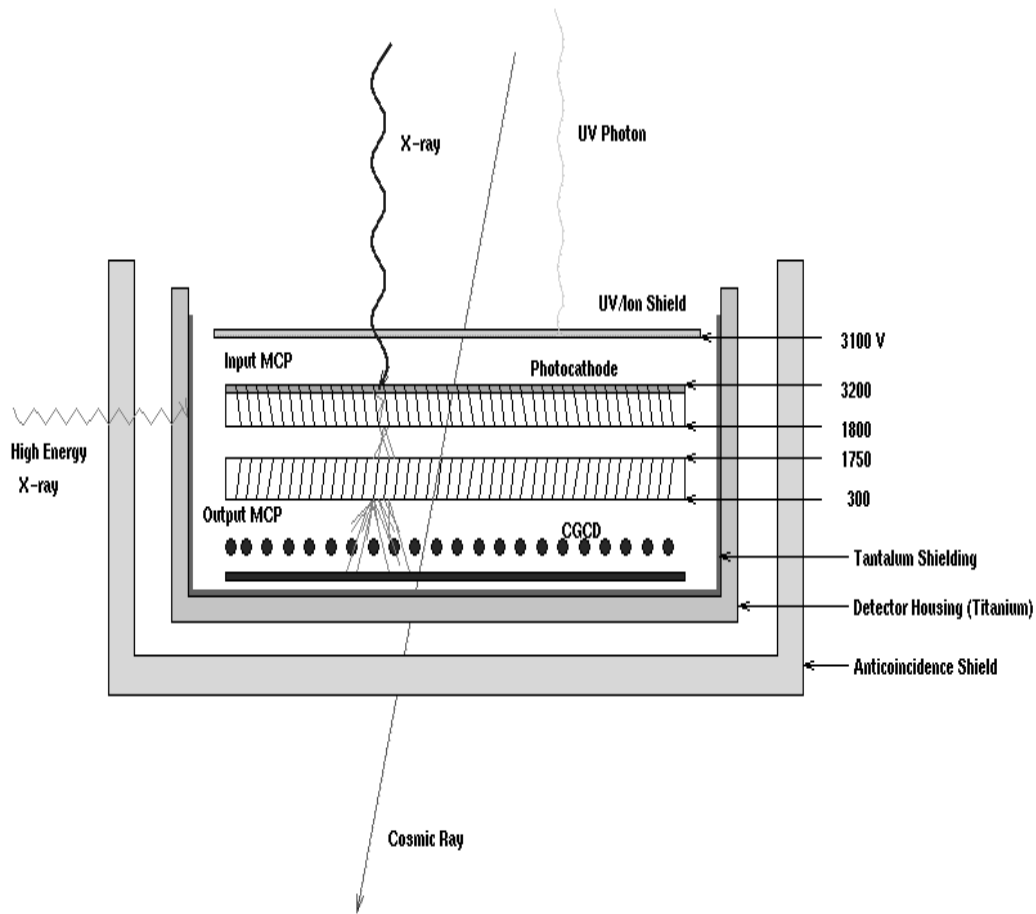


Figure 2: Schematic representation of HRC type detectors showing UV ion shield, photocathode, chevron pair of MCPs Crossed Grid Charge Detector (CGCD) readout and shielding.

measured for out-of-band UV transmission. A plot of the measured X-ray transmission of the HRC-I UVIS witness samples, as well as a model of the transmission is presented in Figure 3. A more detailed description of the UVIS tests, and of the HRC UV ion shields in general, are presented elsewhere in these proceedings ¹¹.

2.2 PHOTOCATHODE

To enhance Quantum Efficiency (QE) a $\sim 14000\text{\AA}$ CsI photocathode was vacuum evaporated on to the input face of the top MCP. The resulting photocathode enhances quantum efficiency; however, it is susceptible to damage from exposure to humid air. For this reason, the CsI coated HRC MCPs are continually either under vacuum or in a dry nitrogen atmosphere. The QE of CsI coated HRC type MCPs has been extensively tested for the purpose of modeling the response of the HRC instruments. This testing included quantum efficiency measurements while scanning across the CsI edges of coated MCPs at the Daresbury Synchrotron Light Source.¹⁵

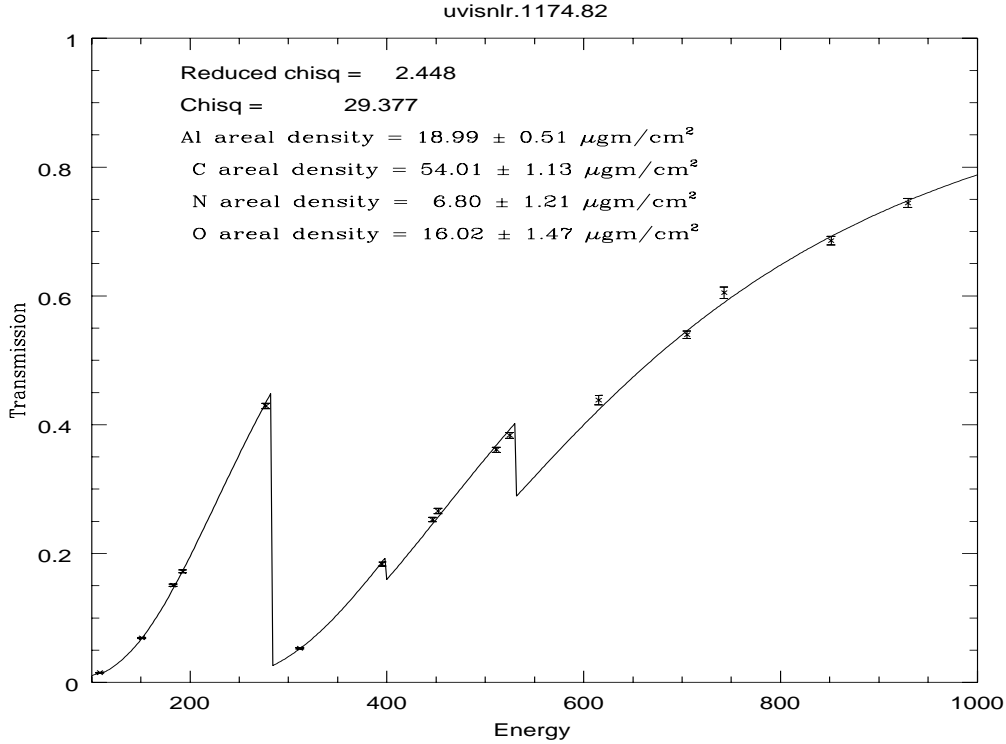


Figure 3: X-ray transmission measurements and model of the HRC-I UV ion shield. Measurements were performed on witness samples of the actual HRC-I UVIS.

2.3 MICROCHANNEL PLATES (MCPs)

The HRC-I MCPs are 100mm \times 100mm square. They have 10 μm pores on 12 μm centers. Both the top and bottom MCPs were cut to give the pores a 6 $^\circ$ bias angle. The MCPs have a nominal $L : D$ ratio of 120 : 1. The 6 $^\circ$ bias angle on the input face has been shown to optimize the detector QE when averaged over the HRMA cone angles. The HRC-I Microchannel Plates (MCPs) were manufactured by the Galileo Electro Optics Corporation (GEOC) in Sturbridge, MA. These MCPs are manufactured from a proprietary low internal radioactivity glass. Prior to selection, candidate flight MCPs underwent a rigorous inspection and testing program.¹⁰

2.4 THE CROSSED GRID CHARGE DETECTOR (CGCD)

The electron charge cloud exiting the rear of the output MCP is collected by two orthogonal grids of gold alloy wires. These wires are separated and held in place by a laser-ruled alumina ceramic block. Beneath the two planes of wires is a deposited gold reflector plane which is biased to ensure $\approx 100\%$ collection of the charge cloud. The grid wires are nominal 100 μm diameter on 200 μm spacing. Each wire is connected to its nearest neighbor with a 10 $k\Omega$ resistor. Every eighth wire is then connected to a charge sensitive amplifier. There are 64 of such amplifiers for each axis. The output face of the rear MCP is attached to a separate “MCP trigger” charge amplifier. This “MCP trigger” amplifier senses the exit of the charge cloud and is then used to trigger the electronics.

The X-ray position is determined by calculating the centroid of the charge cloud exiting the rear MCP via the

“three tap algorithm”. In short, the three tap algorithm determines the charge cloud centroid using a combination of digital and analog electronics and off-line processing. Fast discriminators and logic circuits first determine a “coarse” position, which is the amplifier with maximum detected charge. Analog switches then select the three amplifiers centered on that coarse position and steer them to analog to digital converters. The coarse position and 3 digitized values are then used off-line to calculate the event position. This process is performed for each axis.

It has been demonstrated that the three tap algorithm maintains high imaging capability while minimizing the effect of electronic noise. Further discussions of the HRC electronics and the three-tap positioning algorithm have been discussed elsewhere.^{16,17}

2.5 BACKGROUND AND SHIELDING

The HRC is by design a faint object camera. As such, the detectors have been optimized to have a minimum background counting rate. The intrinsic background counting rate has been minimized by constructing the HRC of materials with low radioactive content. In particular MCPs fabricated from glass without potassium or rubidium have resulted in background reductions > 10 over previous MCP glass formulations.¹⁰

Both active and passive shielding are employed to minimize external sources of background radiation.

Tantalum sheet metal is used around the HRC instruments to minimize the response of the detector to out-of-band $\sim 20\text{keV}$ gamma rays. A plastic scintillator anticoincidence detector is also used to veto cosmic ray events which trigger the HRC.

Background counting rates of the HRC detectors are expected to be to $\approx 4 \times 10^{-6} \text{sec}^{-1} \text{arcsec}^{-2}$ in orbit.

3 CALIBRATION

To fulfill the scientific goals of the HRC mission, a thorough calibration program was planned. This program was intended to calibrate the HRC/AXAF at various levels of integration from subassembly up through an end-to-end calibration encompassing the HRMA, the OTGs and the detectors. The subassembly testing was to be performed at Smithsonian Astrophysical Observatory (SAO) laboratories in Cambridge MA prior to shipping the completed instrument to the X-ray Calibration Facility (XRCF) at Marshall Space Flight Center (MSFC) in Huntsville AL. “End-to-end” testing at XRCF was to determine the Effective Area of the HRC instruments in conjunction with the HRMA and the OTGs for both on and off axis. Point Spread Function (PSF) of the instrument/HRMA was to be determined as well as count rate linearity and spatial linearity.

The subassembly plan¹⁸ was to include detailed testing and calibration of the UVIS characteristics, including uniformity, X-ray and UV transmission. The QE of the HRC detectors was to be determined at 22 discrete energies and at various angles of incidence. These angles of incidence were to encompass the cone angles of the HRMA. The HRC resolution, spatial linearity, count rate linearity were also to be determined. These calibration data were then to be incorporated into empirical models of the HRC performance. Due to scheduling pressure to complete and deliver the final HRC, only a fraction of the original calibration was accomplished. During final assembly, some additional design modifications were also implemented to accommodate the incorporation of all the additional flight hardware; namely it was decided that it would be necessary to operate with the UVIS at ground potential as opposed to the original +100 volts wrt to the top MCP. Some laboratory tests were performed with non-flight HRC detectors to examine the effects of this late design change and at that time none were observed.

Upon delivery of the flight HRC to XRCF for end-to-end testing, several problems were discovered. First, a very high amplitude 90kHz ripple was observed from the high voltage power supplies. This ripple was present on the trigger signal for the HRC and necessitated operating the HRC at a much higher trigger threshold. This higher trigger threshold resulted in much lower effective HRC QE values, especially for the HRC-S detector. Second, a small “ghosting” in the PSF was observed primarily in the HRC-I detector. Later it was determined that the PSF “ghosting” was due to operating the UVIS at ground potential. This phenomenon is still being investigated. Third, the MCPs showed a higher than expected gain causing some pulse-height saturation.

Following the XRCF calibration, the gain saturation problem was fixed and the HRC was returned to the SAO laboratories in Cambridge, MA. At SAO, the HRC detectors were calibrated for absolute quantum efficiency and spatial uniformity. Furthermore, at this time the HVPS ripple was fixed by installing some filter networks into the high voltage power supplies. The detector modifications are discussed elsewhere in these proceedings.¹⁹

After flat field testing of the HRC at SAO, the HRC was returned to XRCF for vibration and thermal-vacuum testing. During the last stages of thermal-vacuum testing, the HRC was tested for off band response to visible and UV light.

The following sections will describe the tests and results obtained at XRCF and at the HRC laboratories at SAO. The results will be limited to the discussion of the HRC-I detector. Discussion of the HRC-S results is presented by Kraft *et al*²⁰ elsewhere in these proceedings.

3.1 XRCF CALIBRATION OF THE HRC-I

For the purposes of using the HRC-I on AXAF for astronomical investigations, several quantities are of primary interest. These quantities are: the effective area of the HRC-I in conjunction with the HRMA; the point spread function (PSF) of the HRC-I in conjunction with the HRMA; and the count rate linearity of the HRC-I. This paper will now briefly describe the XRCF facility and it will present preliminary results determined from data obtained there.

3.1.1 THE FACILITY

The X-ray calibration Facility, depicted in Figure 4, consists of an X-ray Source System (XSS), a long $\sim 500\text{m}$ pipe and an $\sim 23\text{m}$ long $\times 7.3\text{m}$ diameter instrument chamber. In addition there is an X-ray beam monitoring station 38m from the XSS. The features of the XRCF were optimized for calibrating AXAF. The XSS consists of several X-ray sources, namely: an Electron Impact Source (EIPS); a tungsten Rotating Anode Source (RAS) with Double Crystal Monochromator (DCM); a Penning Source and a RAS with a High Resolution Erect Field Spectrometer (HIREFS). The EIPS was used with various anode-filter combinations to produce characteristic X-ray lines. The DCM provided X-rays from ~ 1.5 to 10 keV. The HIREFS, a grating monochromator provided X-rays from $\sim 300\text{eV}$ to 2 keV. For the purpose of HRC-I testing only the DCM, the HIREFS, and the EIPS with Be, B and C anodes were used.

In addition to the sources, the XRCF employed six X-ray detectors for monitoring the beam during the calibration. Four of these detectors were flow proportional counters (FPCs) located near the front of the HRMA. Two other detectors, a Solid State Detector (SSD) and another FPC were located $\sim 38\text{m}$ from the XSS. The SSD was used to monitor the beam flux and this FPC was used to monitor and spatially map the beam. A detailed discussion of the capabilities of the XSS have been presented elsewhere.²¹

During calibration, the the orientation of the HRMA was changed in pitch and yaw to simulate the performance of the AXAF telescope to off axis illumination. In addition various quadrants of the HRMA could be occulted

to determine the location of best focus.

The HRC was attached to a Five Axis Mount (FAM). This FAM provided instrument selection, instrument motion and focusing. During long in-focus measurements, the FAM executed a small scale serpentine motion to prevent damage to the detectors due to excessive localized charge extraction. The majority of the other calibration data were taken with the instruments slightly out of focus for the same reason. In flight, spacecraft “dither” will provide the same function.

3.1.2 EFFECTIVE AREA (EA)

The Effective Area (EA) of the HRC-I/HRMA is the ratio of the HRC-I count rate to the input X-ray flux at the HRMA. The EA is a product of the HRMA effective area, the UVIS transmission and the CsI coated MCP efficiency. Structure in the HRC-I/HRMA EA is therefore evident at energies of the iridium, carbon, cesium and iodine edges. The number and spacing of EA measurements were made with the locations of these edges in mind.

Data to determine the Effective Area (EA) of the HRC-I with the HRMA were collected with the EIPS, DCM and the HIREFS sources. For this preliminary analysis only EIPS and DCM data are presented. The HIREFS source had a complicated spectrum with large higher order contamination. In addition the HIREFS beam uniformity at the input of the HRMA showed considerable non-uniformity. For these reasons, analysis of HIREFS data will be complex and is still incomplete.

To perform an EA measurement, the HRC-I was illuminated for a fixed period of time to ensure that a minimum 10,000 photons of the desired energy were collected. Simultaneously, the count rate in the four flow proportional counter BNDs located near the input of the HRMA was recorded. In off-line analysis the photon flux at the HRMA was determined from the BND data and preliminary models of the actual FPCs. From the photon flux and the HRC-I rates, the EA was then determined. Both on and off axis EA measurements were made.

The preliminary on axis measurements of EA for the HRC-I versus expected EA is presented in Figure 5. Effective area versus off axis angle for various energies is presented in Figure 6. The drop in EA with increasing off-axis angle is due primarily to the geometric vignetting of the telescope.

3.1.3 COUNT RATE LINEARITY (CRL) AND POINT SPREAD FUNCTION (PSF)

During the XRCF calibration, several tests to determine the in focus Count Rate Linearity (CRL) of the HRC-I were performed. The purpose of these tests was to determine whether the HRC-I count rate was linear with incident flux over a limited range of values. Non-linearity in count rate versus flux for MCP detectors is primarily caused by the finite re-charge time of the illuminated MCP pores. This re-charge time depends on MCP resistivity and the area of illumination.

The CRL measurements at XRCF were performed with the HRC-I in focus and with no FAM motion. The absence of FAM motion limited the allowable rate and total exposure of the HRC-I. Beam flux was monitored by the 4 BND detectors near the input face of the HRMA. The count rate of these BNDs are linear up to rates > 10kHz.

The lack of FAM motion ensures that the data are free of any systematics introduced by the FAM positioning system. This CRL data can then be used to determine the HRC-I/HRMA point spread function albeit with limited statistics.

Count Rate Linearity versus BND rate is presented in Figure 7. The HRC-I/HRMA was illuminated with 2.56

keV X-rays from the DCM source. No evidence of nonlinearity over the limited flux values is evident.

The PSF was determined from a second set of CRL data taken with a carbon anode in the EIPS source. The preliminary results for these PSF measurements are presented in Figures 8 through 10. Orthogonal slices through the center of the PSF were fit to a Gaussian and the Encircled Energy (EE) versus radius was determined. The FWHM of the PSF slices are $47.3\mu\text{m}$ and $43.9\mu\text{m}$. The half power radius for the EE is $22.5\mu\text{m}$.

This PSF analysis was performed with limited statistics and no effort was made to eliminate effects of gravity sag on the HRMA. Final PSF data still needs to be deconvolved from FAM motion and from the HRMA response .

As previously discussed, during flight assembly of the HRC instrument it was decided to operate the HRC detectors with the UVIS at ground potential. As a result, the UVIS to MCP potential changed from +100V to $\sim +3000\text{V}$. Subsequent testing at SAO has shown that this change is responsible for producing a faint, $\approx 1\%$ “ghost” image slightly displaced in one direction from the true PSF image. This phenomenon is currently being investigated.

3.2 FLAT FIELD TESTING

Following calibration at XRCF, the HRC instrument was returned to the SAO HRC laboratory in Cambridge, MA for hardware modification and uniform field X-ray illumination. The uniform field X-ray illumination was done to determine the absolute Quantum Efficiency of the HRC detectors as well as their spatial uniformity of response. The SAO facility was better suited than XRCF for such testing on account of the higher X-ray flux levels attainable.

3.2.1 THE FACILITY

The SAO HRC laboratory is depicted in Figure 11. The facility consisted of a Manson model 5 multi-anode X-ray source, two Manson 04 flow proportional counters and a $\approx 7\text{m}$ long evacuated X-ray pipe. The HRC instrument was mounted to the end of the pipe with a series of different fittings. Each fitting was tailored so that the HRC-I detector and the HRC-S segments could each be uniformly illuminated. At the same time, this setup allowed full access to the HRC electronics for diagnostics and modification. During this testing a temporary modification to the HRC electronics was implemented that allowed data rates $10\times$ greater than normal HRC event telemetry rate of $\approx 188\text{sec}^{-1}$.

3.3 UNIFORM ILLUMINATION AND SPATIAL UNIFORMITY OF THE HRC-I

X-ray illumination was provided with a Manson model 5 multi-anode electron impact source. The anodes and filter combinations listed in Table 1 were used for the HRC-I detector flat field illumination tests.

During the uniform field illumination tests, the HRC was exposed for a fixed period of time so that a minimum 10×10^6 photons were detected for all anodes excepting boron, for which 3×10^6 photons were detected; low flux levels from boron would have necessitated excessive integration times.

The beam flux close to the input of the HRC was measured using one of the Manson 04 flow proportional

counters which was mounted on a retractable arm. This Beam Normalization Detector (BND) was not operated concurrently with the HRC on account of the slow gas leak through the thin flow counter window and the proximity of the detector to the HRC.

Absolute flux measurement and temporal monitoring were performed by first “cross-calibrating” the BND to a second Monitor Detector (MD) close to the X-ray source. With the HRC off, the BND was inserted into the center of the beam; the BND and the MD flow proportional counter were then operated concurrently and cross-calibrated.

During the flat field illuminations of the HRC, the BND was evacuated and retracted from the beam. The MD was operated to monitor the temporal stability of the beam and by using the BND to MD cross-calibration, the photon flux at the input of the HRC was determined.

In off-line analysis, the photon flux at the input of the HRC was used to determine the absolute Quantum Efficiency (QE) of the HRC-I detector. In addition the spatial uniformity of the HRC-I detector response was measured.

Line	Energy	Filter	MFPs	V_A	L/C
B $K\alpha$	183 eV	7 μ parylene-C	5.87	600 V	48.4
C $K\alpha$	277 eV	33 μ polypropylene	5.94	1000 V	171
O $K\alpha$	525 eV	2 μ Cr	4.67	1000 V	29.3
Ni $L\alpha$	851 eV	2 μ Cu	3.80	2500 V	2.55
Al $K\alpha$	1487 eV	50 μ Al	5.40	4000 V	38.9
Ag $K\alpha$	2984 eV	10 μ Ag	4.86	6000 V	0.60
Ti $K\alpha$	4511 eV	150 μ Ti	6.80	10000 V	6.73
Fe $K\alpha$	6404 eV	125 μ Fe	6.97	10000 V	1.78

Table 1: Summary of line energies, filters, thicknesses, anode voltages, and predicted line-to-continuum ratio of the X-ray source for HRC-I flat fields.

The absolute QE at the eight energies are presented in Table 2 and Figure 12. These values are averages over the entire CsI coated HRC-I active area.

HRC-I QE		
Element	Energy (eV)	QE
B	183	0.062
C	277	0.19
O	525	0.11
Ni	851	0.26
Al	1487	0.28
Ag	2980	0.093
Ti	4511	0.10
Fe	6404	0.13

Table 2: QE of HRC-I averaged over entire detector. $\sim 10^7$ photons collected for all energies except $\sim 3 \times 10^6$ for B (183)eV.

Surface plots of the detector flat field response, and of the average gain for the HRC-I detector at one of the energies (1.48keV), are presented in Figures 13 and 14. The detector efficiency is seen to be uniform at the $\sim 10\%$ level even though the detector gain shows considerable variation.

The inherent energy resolution of the HRC-I detector was investigated by examining the effect of incident X-ray energy on detected pulse height. The detected pulse height of the HRC-I versus incident energy is presented in Figure 15. It is evident that the HRC-I has some limited energy resolution for an ensemble of photons, particularly at energies $< 1\text{keV}$.

3.4 COMPARISON OF XRCF VERSUS FLAT FIELD DATA

As discussed previously, some hardware modifications were done on the HRC instrument after the XRCF calibration. These changes allowed the HRC detectors to operate at lower thresholds and therefore to have a higher quantum efficiency. The resulting higher QE of the HRC-I increases the EA values as measured at XRCF. Using a model of the HRMA mirror area the QE of the HRC-I detector at XRCF was calculated. A comparison of the QE derived from the uniform illumination measurements to the QE derived from the XRCF data is presented in Figure 16

This data shows that the QE, and hence EA of the HRC-I/HRMA has increased by ~ 15 to 25% at low energies due to the post-XRCF hardware changes. Further discussions of these changes have been presented elsewhere in these proceedings.¹⁹

3.5 UV/OPTICAL SENSITIVITY MEASUREMENTS

During HRC thermal-vacuum tests, the HRC detectors were tested for sensitivity to off band UV and optical radiation. These tests consisted of illuminating the detectors to radiation from several calibrated light sources and measuring the response. The light sources were: a mercury lamp with 2537\AA filter; a mercury lamp with a 1850\AA filter; a xenon light/filter at 1470\AA ; and a tungsten-halogen light filtered at 4500\AA . The sources were calibrated at SAO to $\sim 10\%$ using a NIST calibrated photodiode. The measured and predicted response is indicated in Figure 17. Also shown is the HRC-I specification for maximum sensitivity. The predicted response of the detector is a product of the transmission of the UVIS and the photocathode sensitivity. The UVIS transmission model was determined from laboratory measurements and from published optical constants. Photocathode response was estimated from previously reported measurements. The uncertainty in the resulting model of HRC-I response is large. No gross leaks through or around the UVIS were detected.

4 CONCLUSIONS AND DISCUSSION

Preliminary results from the HRC-I calibrations at XRCF and at the HRC laboratories have been presented. These results included effective area, point spread function, count rate linearity, absolute QE and uniformity of the HRC-I detector. The imaging performance of the HRC-I/HRMA detector has been shown to be < 1 arcsec and EA measurements were close to expectations.

Systematic errors, particularly beam normalization detector models, FAM motion, and uniformity of the X-ray beams at the input face of HRMA at XRCF will have to be studied in great detail before final calibration data is presented. In addition, the effects of the hardware modifications on the HRC detectors will have to be examined further, and the resulting performance changes will have to be combined with XRCF data to generate

final models of the HRC-I/HRMA effective area.

5 ACKNOWLEDGEMENTS

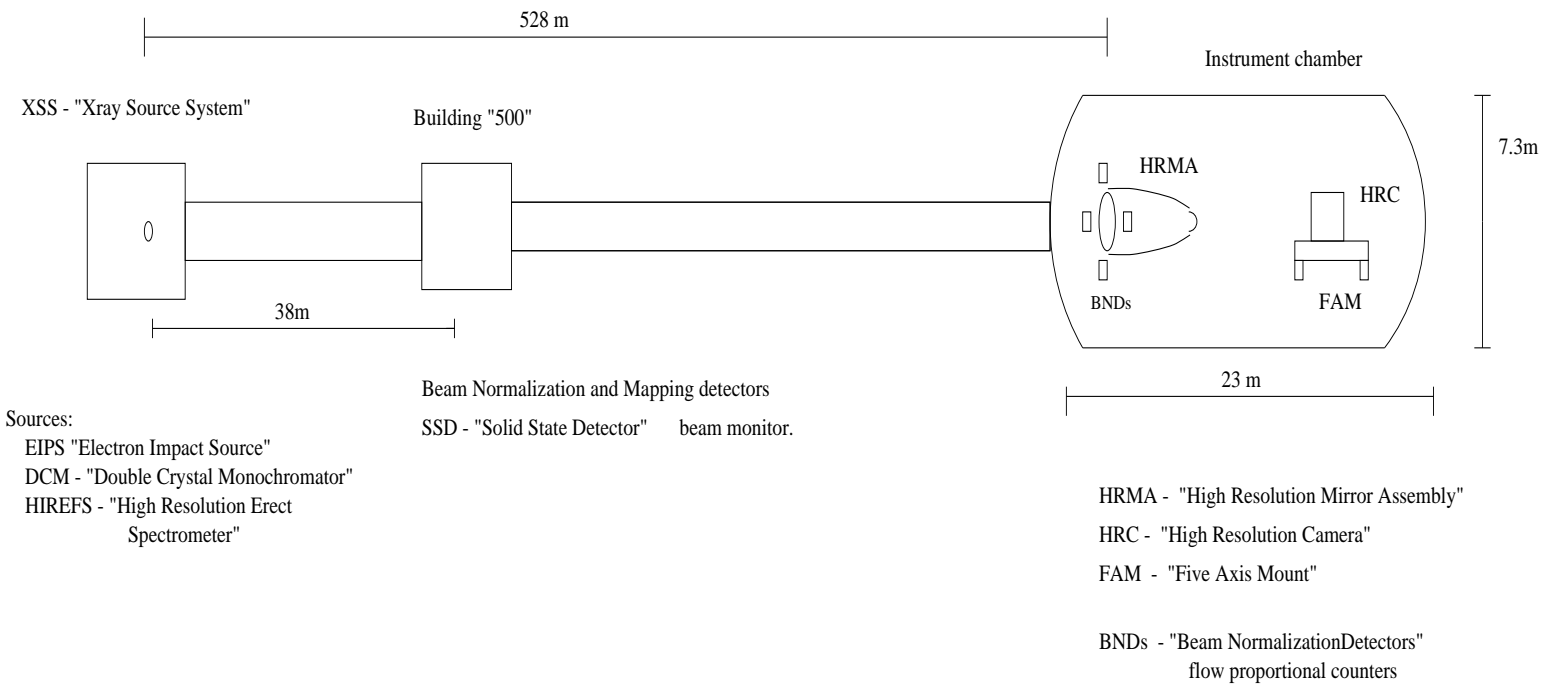
We are grateful for the support of Gerry Austin, Jack Gomes, John Polizotti, Richard Goddard, Joe D'Arco, Frank DeFreeze, Desi Hamvas, Frank Rivera and Peter Warren. This work has been supported by NASA contract NAS8-38248 .

6 REFERENCES

- [1] Weisskopf, M.C., "AXAF VETA test: an overview" in *Multilayer and Grazing Incidence X-Ray/EUV Optics for Astronomy and Projection Lithography*, SPIE **1742**, 2, (1992).
- [2] Van Speybroeck, L.P "Performance Expectations versus Reality", SPIE **3113**,(1997).
- [3] Brinkman, A.C., van Rooijen, J.J., Bleeker, J.A.M., Dijkstra, J.H., Heise, J., de Korte, P.A.J., Mewe, R., and Paerels, F., *Astro. Lett. and Commun.*, 26, 87 (1987).
- [4] Markert, T.H., Canizares, C.R., Dewey, D., McGuirk, M., Pak, C.S., Schattenburg, M.L., "High Energy Transmission Grating Spectrometer (HETGS) for AXAF", in *EUV, X-Ray, and Gamma-Ray Instrumentation for Astronomy V*, SPIE **2280**,(1994).
- [5] Zombeck, M.V, "Advanced X-Ray Astrophysics Facility (AXAF)", Proceedings of the International School of Space Science Course on "X-Ray Astronomy", Aquila,Italy,1996 Cfa preprint 4003.
- [6] Weisskopf, M.C., O'Dell, S.L. and Elsner, R.F., "Advanced X-Ray Astrophysics Facility - AXAF an Overview", X-Ray and Extreme Ultraviolet Optics,R.B.Hoover and A.B.C Walker Jr.,eds., Proc. SPIE **2515**,1995.
- [7] Giacconi, R. *et al*, *Astrophysical Journal*,230,1979.
- [8] Zombeck, M.V., David, L.P., Harnden, F.R. Jr. and Kearns, K., "Orbital Performance of the High Resolution Imager (HRI) on ROSAT", SPIE **2518**,(1995).
- [9] Kenter, A.T., Chappell, J.H, Kraft, R.P., Meehan, G.R., Murray, S.S., Zombeck, M.V., Fraser, G.W., "The High Resolution Camera on AXAF", Spectroscopic Detector", SPIE **2808**, (1996).
- [10] Kenter, A.T., Flanagan, K.A., Meehan, G.R., Murray, S.S., Zombeck, M.V., Fraser, G.W., Pearson, J.F., Lees, J.E., Brunton, A.N. and Pearce, S.E. "MCP selection for the HRC on AXAF" SPIE **2518**,1995.
- [11] Meehan, G.R., Murray, S.S., Zombeck, M.V., Kraft, R.P., Kobayashi, K., Chappell, J.H., Kenter, A.T., Barbera, M., Collura, A., Serio, S., Istituto e Osservatorio Astronomico G.S. Vaiana (Italy) "Calibration of the UV/ion shields for the AXAF High Resolution Camera", SPIE **3114**, (1997).
- [12] J.J. Drake, SAO Internal Memo,1997
- [13] Chappell, J.H., Martin, R.K., Murray, S.S. and Zombeck, M.V. "Background Reduction in Microchannel Plates", SPIE **1344**, 176, (1990).
- [14] Meehan, G.R., Chappell, J.H, Kenter, A.T., Kraft, R.P., Kobayashi, K., Murray, S.S., Zombeck, M.V., Barbera, M, Collura, A. "Measurement of the Transmission of the UV ion Shields of the AXAF High Resolution Camera", SPIE **2808**, (1996).

- [15] Pearce, S.E., Lees, J.E., Pearson, J.F., Fraser, G.W., Brunton, A.N., Flanagan, K.A., Kenter, A.T., Barbera, M., Dhanak, V., Robinson, A., Teehan, D. "Synchrotron calibration of Alkali Halide Coated Microchannel Plate Detectors in the 50-350 and 2000-6000 eV Bands", SPIE **2518**, 1995.
- [16] Murray, S.S. and Chappell, J.H., "The AXAF High Resolution Camera", SPIE **982**, 48, (1988).
- [17] Chappell, J.H. and Murray, S.S., "Position Modeling for the AXAF High Resolution Camera", SPIE **1159**, 460, (1989).
- [18] Kraft, R.P., Chappell, J.H., Kenter, A.T., Kobayashi, K., Meehan, G.R., Murray, S.S., Zombeck, M.V., Fraser, G.W., Pearson, J.F., Lees, J.E., Brunton, A.N., Pearce, S.E., "Absolute Quantum Efficiency Calibration of the AXAF High Resolution Camera" Proc. SPIE **2808**, (1996).
- [19] Murray, S.S., Chappell, J.H., Kenter, A.T., Kraft, R.P., Kobayashi, K., Meehan, G.R., Murray, S.S., Zombeck, M.V., Smithsonian Astrophysical Observatory; Fraser, G.W., Pearson, J.F., Lees, J.E., Brunton, A.N., Pearce, S.E., University of Leicester (UK); Barbera, M., Collura, A., Serio, S., Istituto e Osservatorio Astronomico G.S. Vaiana (Italy) "AXAF High Resolution Camera". SPIE **3114**, (1997).
- [20] Kraft, R.P., Chappell, J.H., Kenter, A.T., Kobayashi, K., Meehan, G.R., Murray, S.S., Zombeck, M.V., Smithsonian Astrophysical Observatory; Fraser, G.W., Pearson, J.F., Lees, J.E., Brunton, A.N., Pearce, S.E., University of Leicester (UK); Barbera, M., Collura, A., Serio, S., Istituto e Osservatorio Astronomico G.S. Vaiana (Italy) "Performance and Calibration of the AXAF High Resolution Camera II: Spectroscopic Detector", SPIE **3114**, (1997).
- [21] Kolodziejczak, J.J., Austin, R.A., Elsner, R.F., Joy, M.K., Sulkanen, M., Kellogg, E.M. and Wargelin, B.J., "X-ray Source System at the MSFC X-ray Calibration Facility" Proc., SPIE **2515**, (1995).

Figure 4: X-ray Calibration Facility showing the X-ray Source System, instrument chamber, HRMA and FAM.



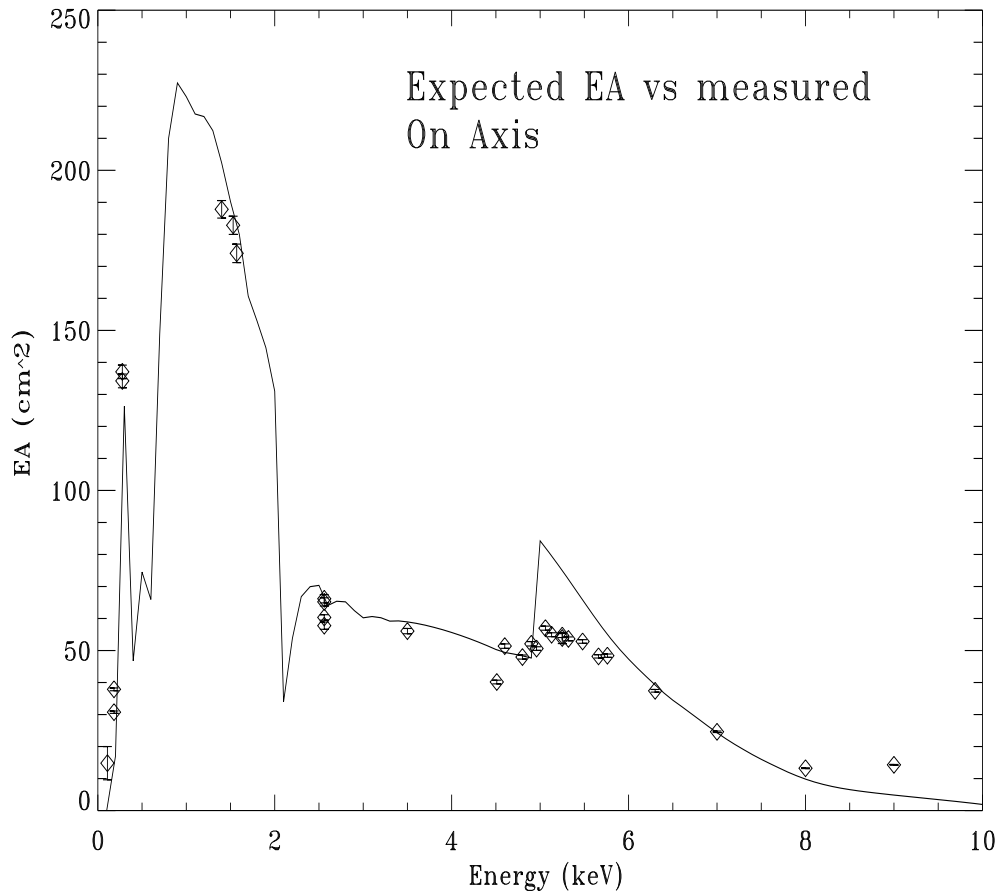


Figure 5: Effective Area of the HRC-I with the HRMA. Each data point represents $\sim 10,000$ photons. Multiple points indicate identical HRMA pitch and yaw on different parts of the detector. Continuous curve is the expected EA prior to XRCF calibration.

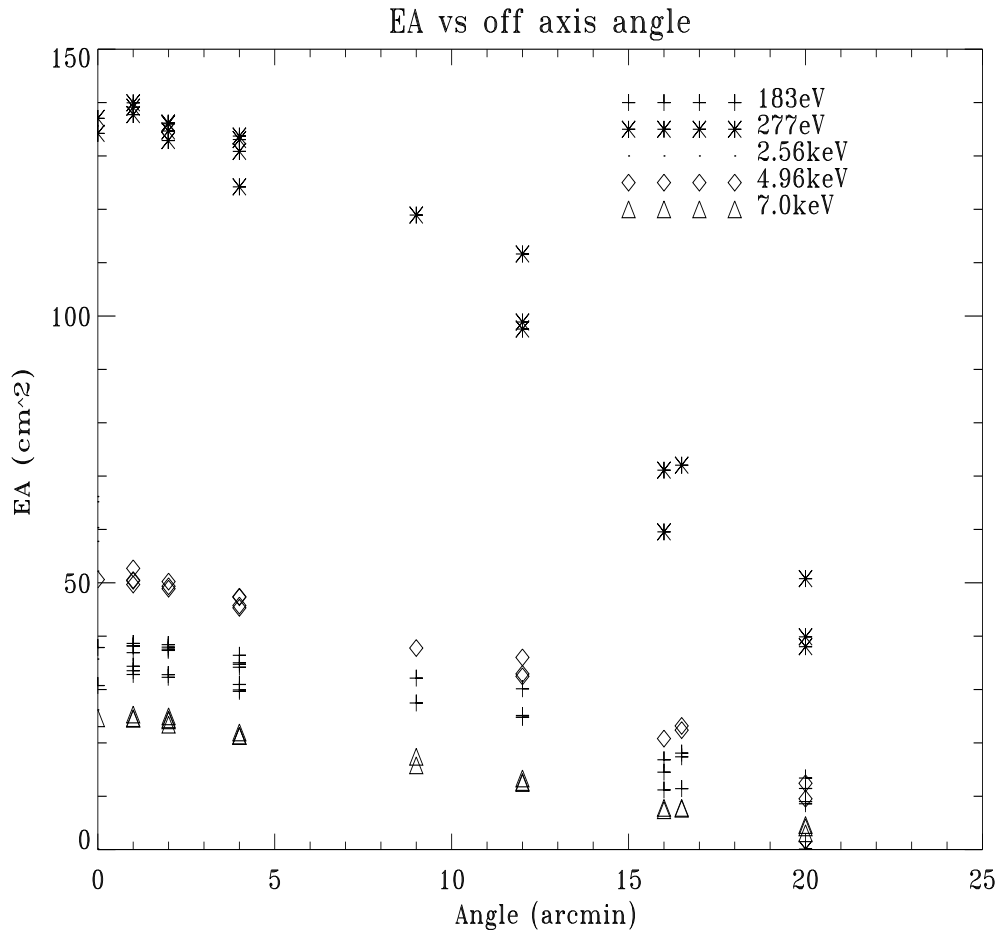


Figure 6: Effective Area of the HRC-I with the HRMA versus off-axis angle. Telescope vignetting is the primary cause of the drop off in EA. Each data point represents $\sim 10,000$ photons. Multiple points indicate identical HRMA pitch and yaw on different parts of the detector.

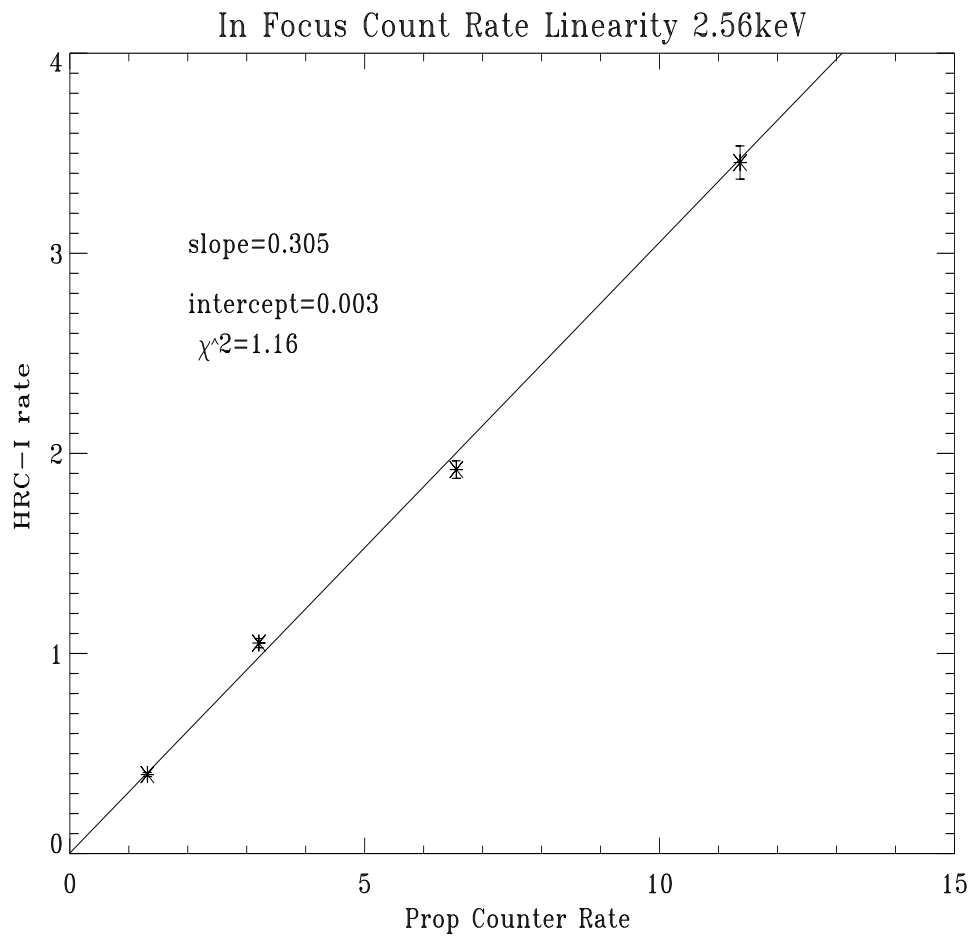


Figure 7: In focus count rate linearity of the HRC-I. Data taken with 2.56keV X-rays from DCM source.

PSF of HRC-I with HRMA

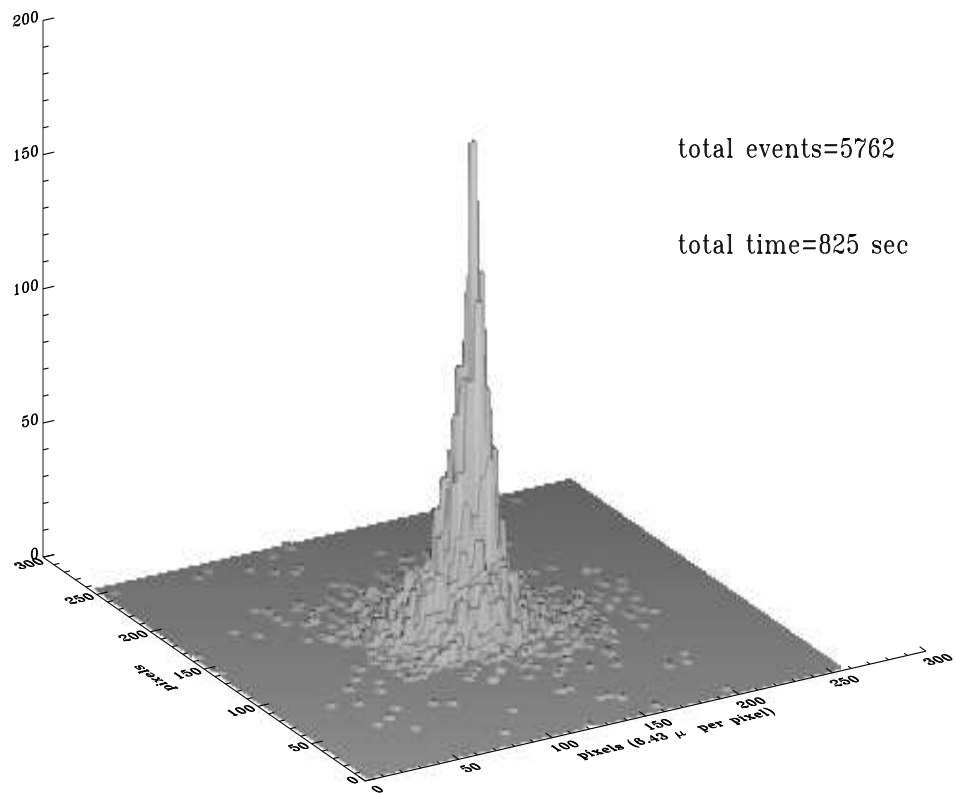


Figure 8: Surface plot of HRC-I point spread function. Data taken with no FAM motion during count rate linearity test. C X-rays at 277eV from EIPS source were used.

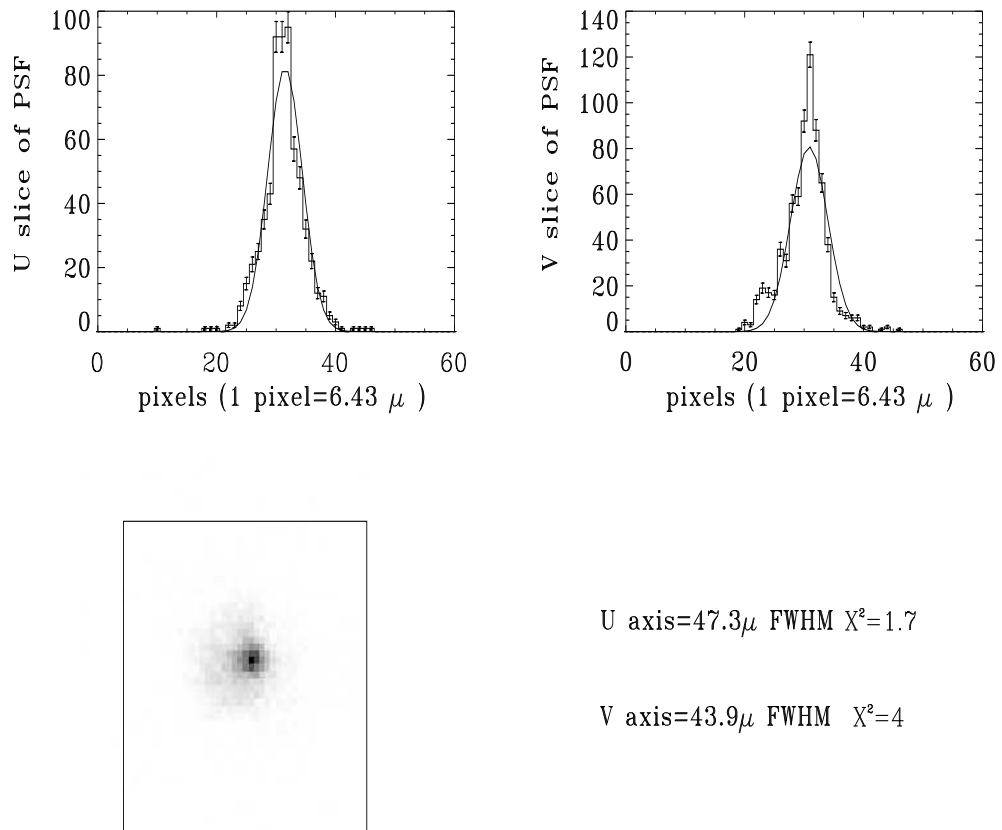


Figure 9: Point Spread Function (PSF) of HRC-I detector. Data taken with no FAM motion during count rate linearity test. C X-rays at 277eV from EIPS source were used.

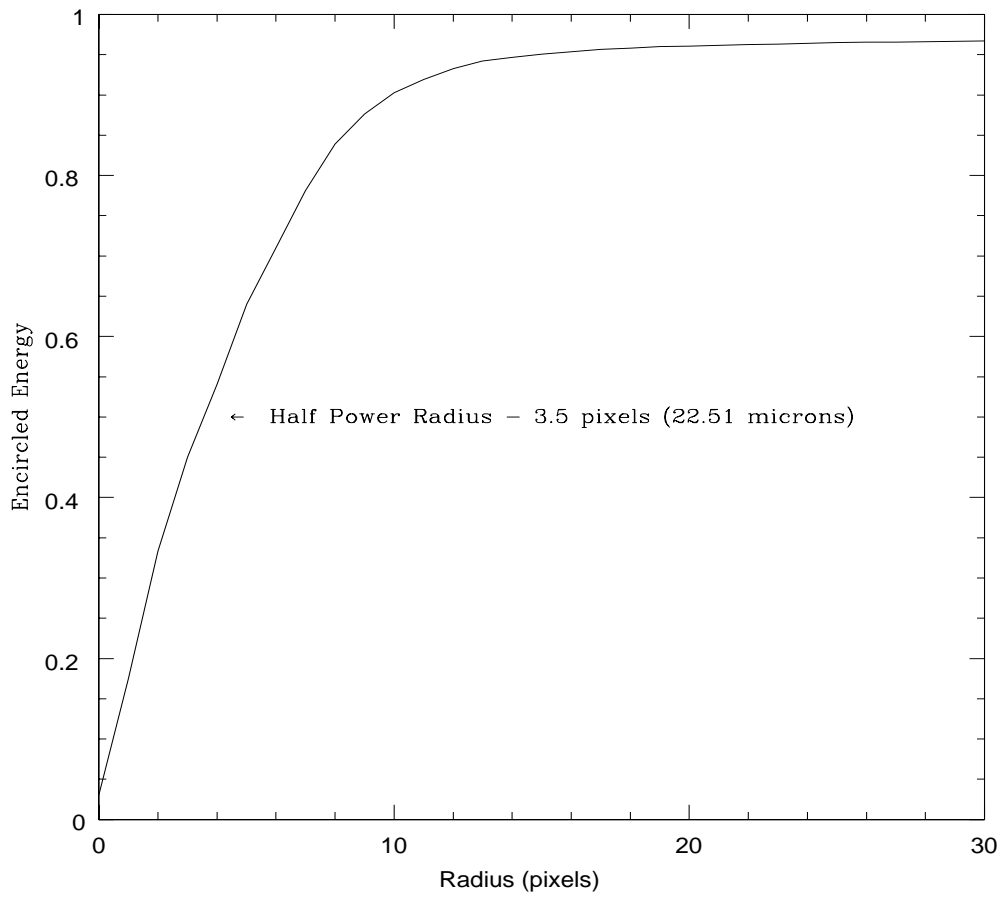
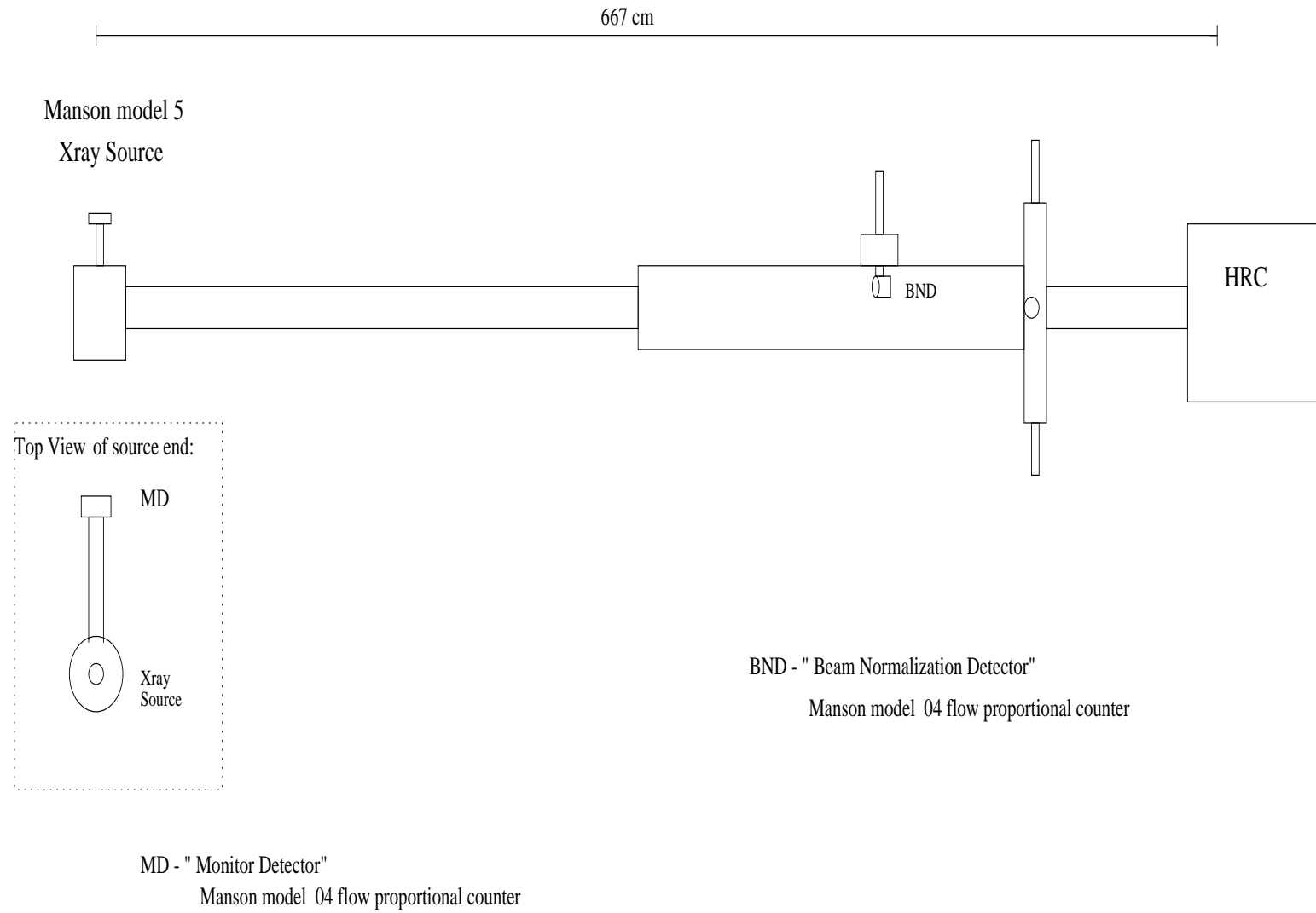


Figure 10: Encircled Energy for the HRC-I point spread function.

Figure 11: Facilities at the SAO HRC laboratory used for flat-field illumination of the HRC detectors.



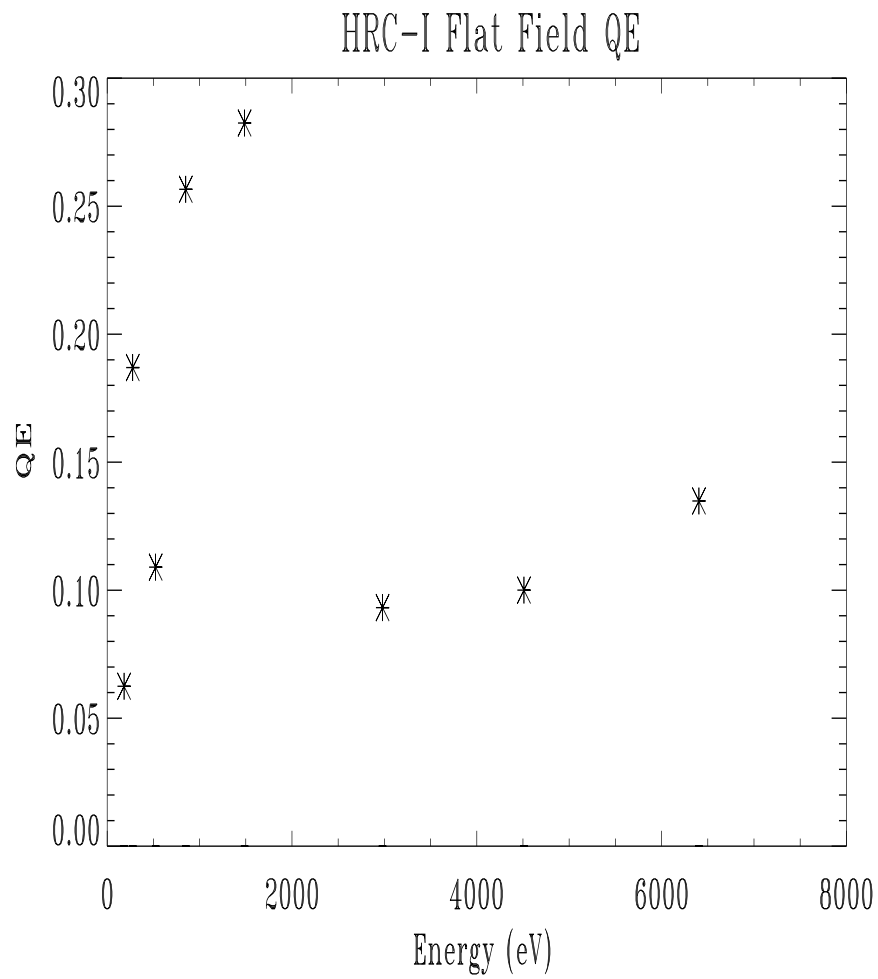


Figure 12: Absolute QE of HRC-I detector versus energy. These values are averages over the entire HRC-I active area. $\sim 10^7$ events were collected for each energy except B (183eV).

Al 1487eV

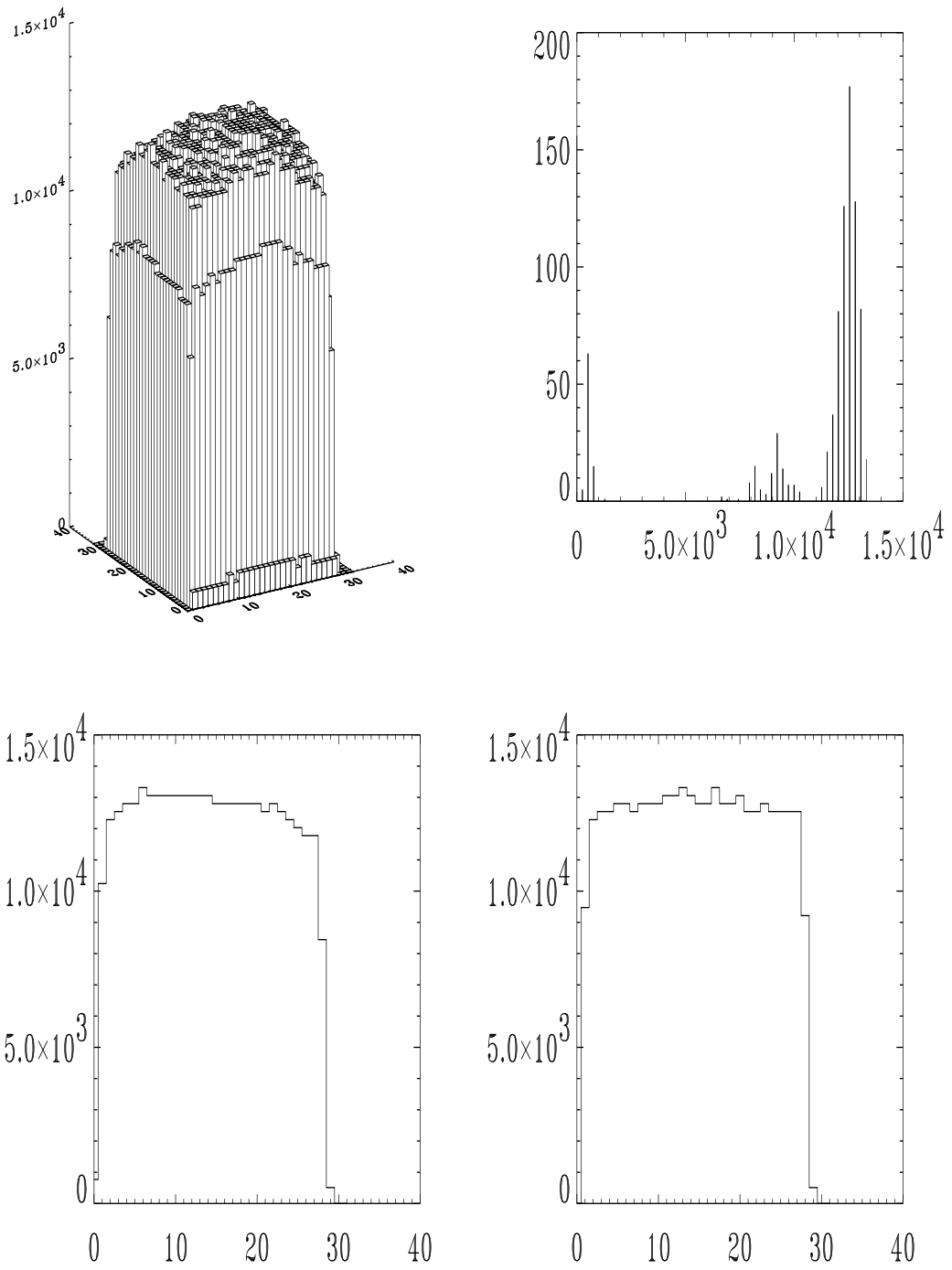


Figure 13: Surface plot of flat field response of HRC-I detector at 1.48keV. The efficiency is uniform at the $\sim 10\%$ level.

Al 1487eV

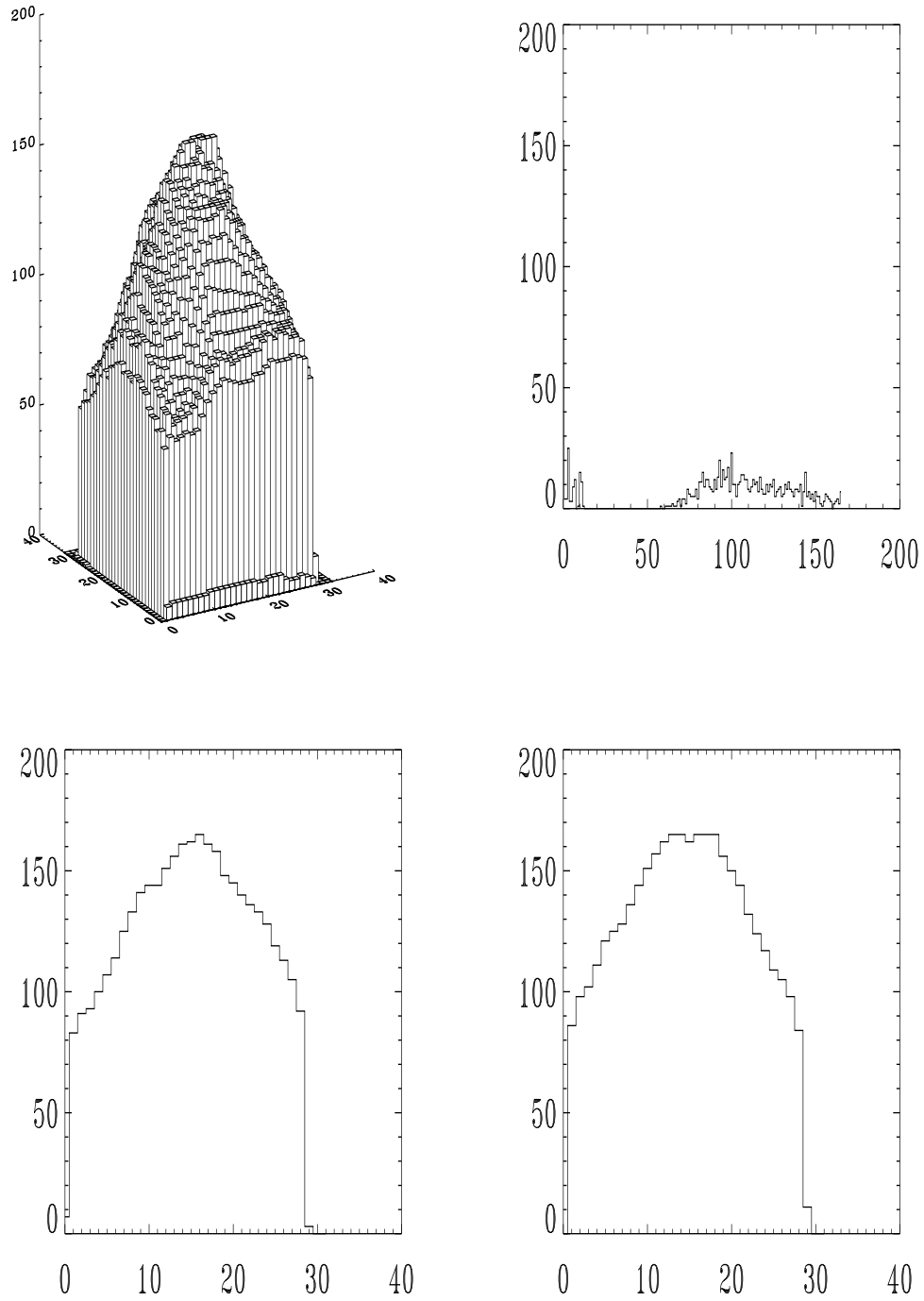


Figure 14: Surface plot of average gain of HRC-I detector at 1.48keV. Large variations in gain over the HRC-I are evident. These large gain variations do not affect the detector efficiency

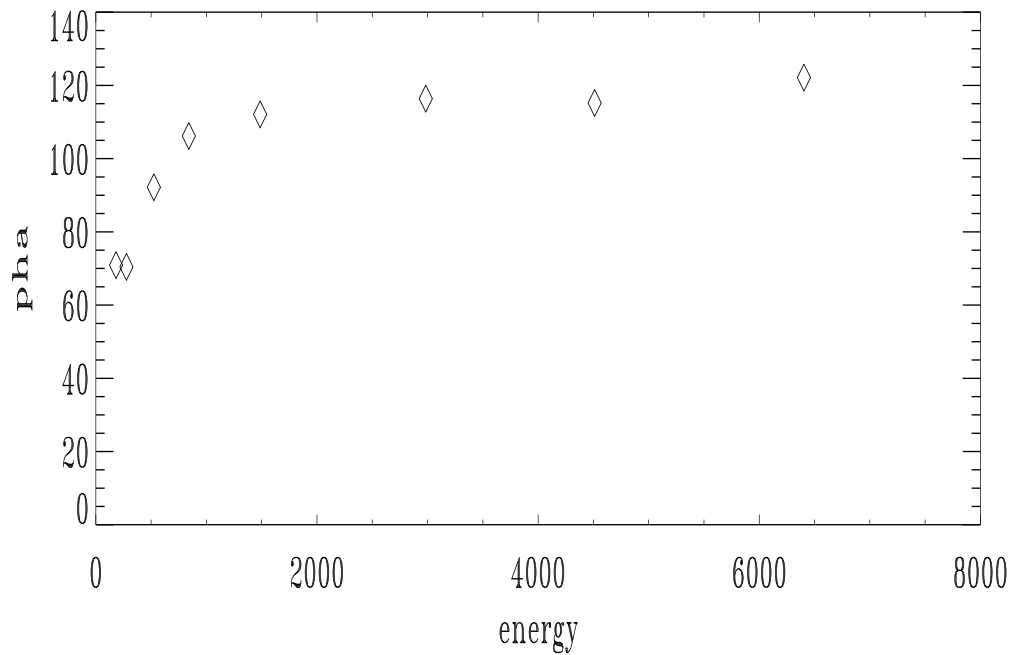
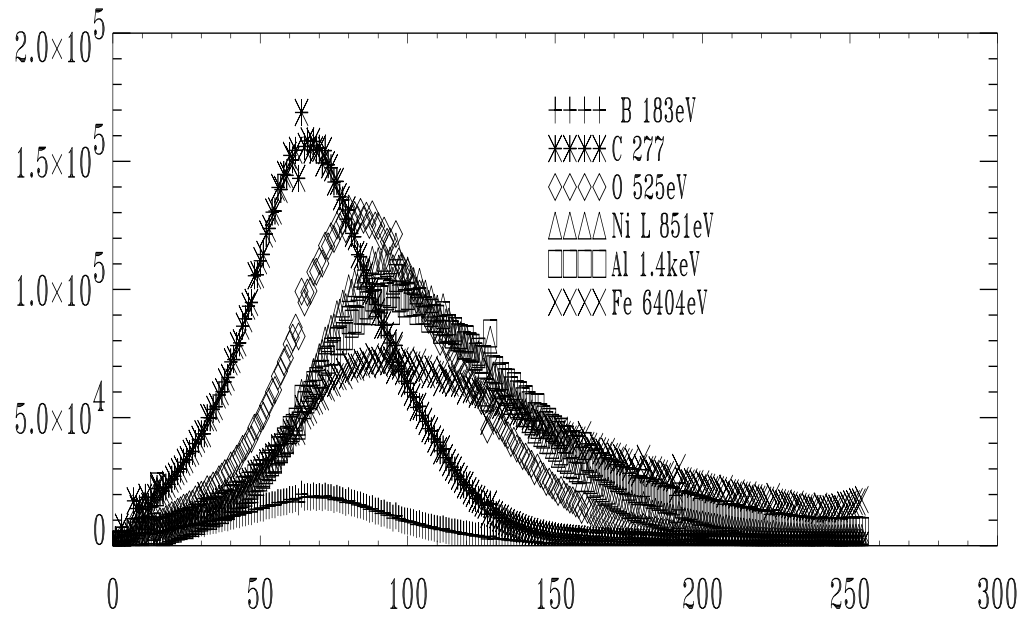


Figure 15: Pulse height distributions versus energy and centroids of pulse height versus energy for the HRC-I detector. It is evident that the HRC-I has some limited inherent energy resolution.

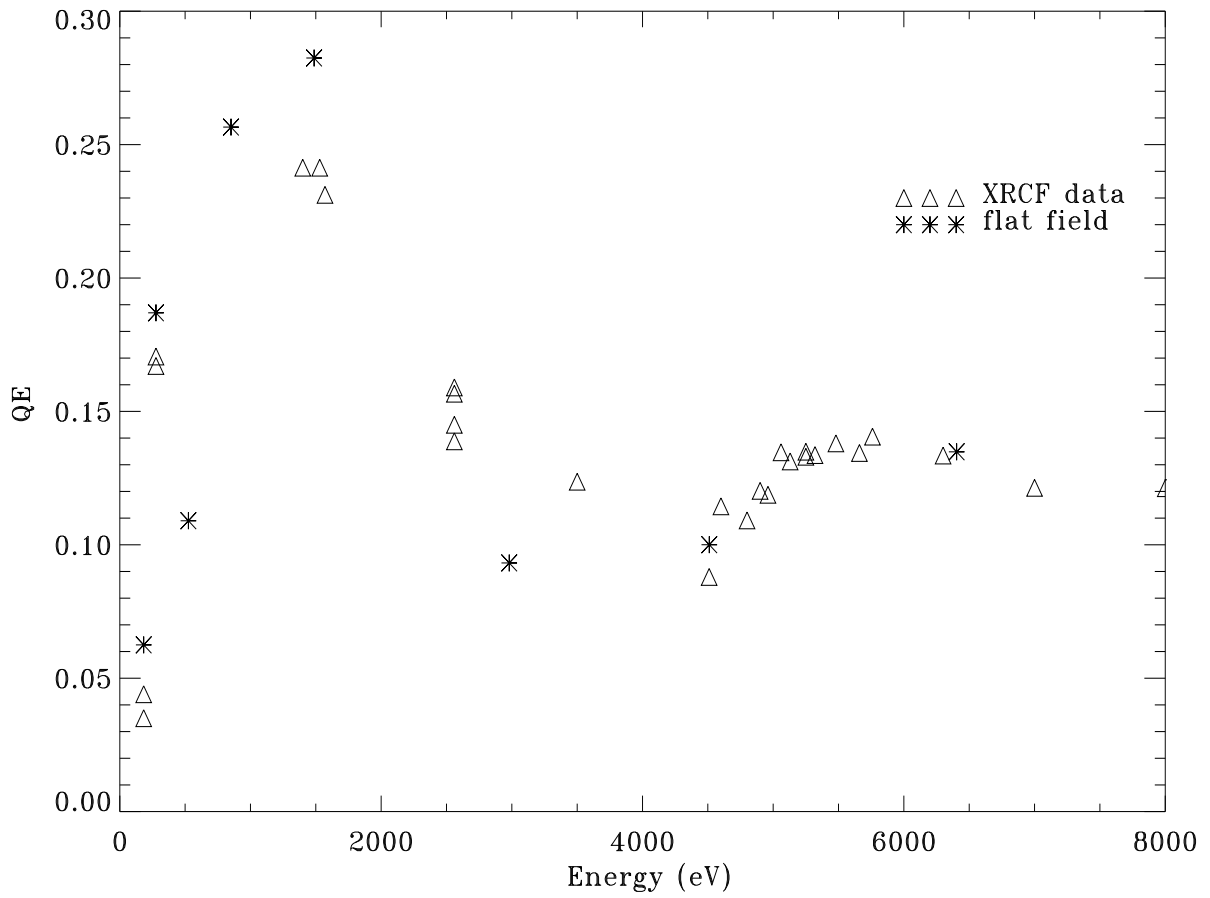


Figure 16: Quantum Efficiency as derived from XRCF Effective Area data and HRMA model versus QE determined during flat field exposures.

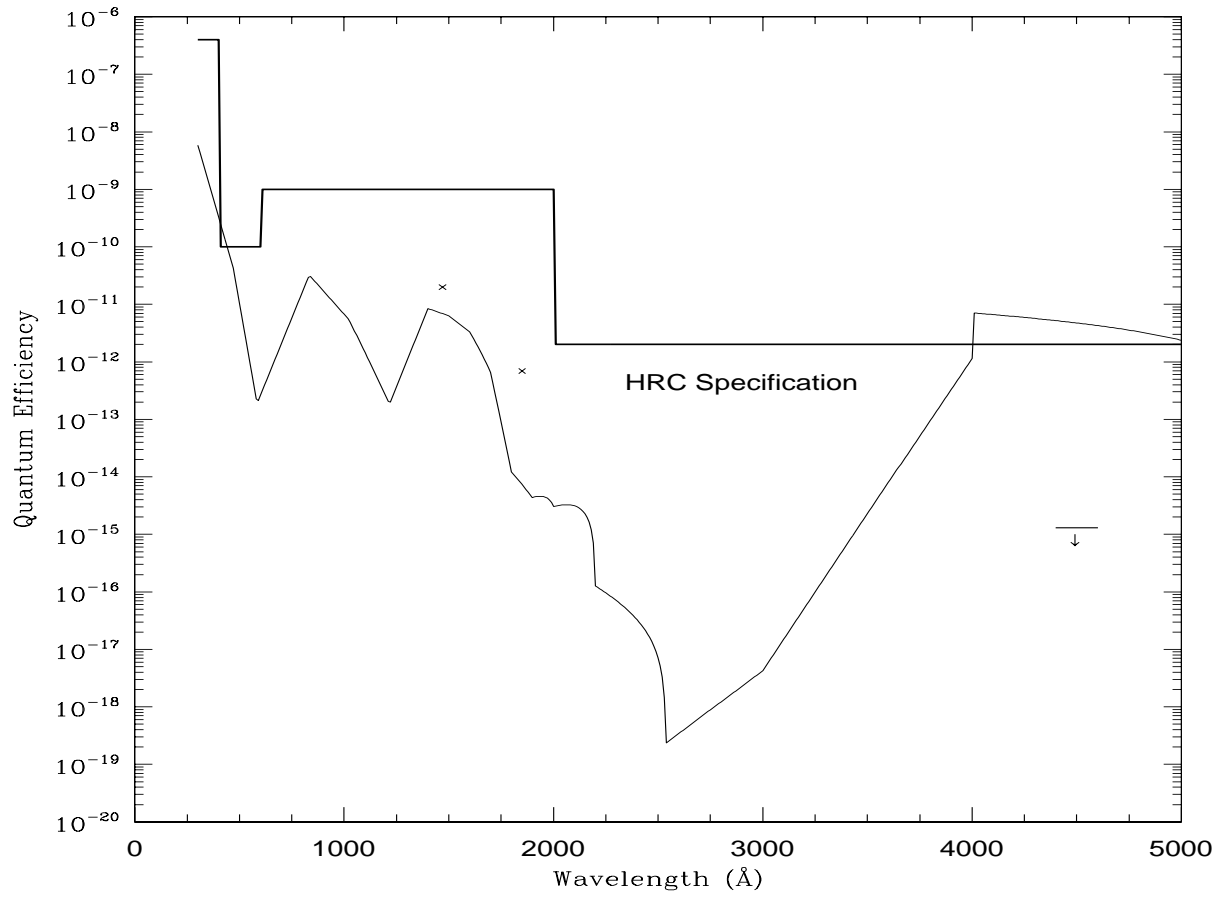


Figure 17: Measured, predicted and specification for UV and optical response of the HRC-I detector. The optical response (4500\AA) is an upper limit.